ACDIV-2022-01
May 2022

Two-dimensional electron beam size measurements with x-ray heterodyne near field speckles

M. Siano, B. Paroli, M. A. C. Potenza, L. Teruzzi, U. Iriso, A. Nosych, E. Solano, L. Torino, D. Butti, A. Goetz, T. Lefevre, S. Mazzoni, G. Trad

Abstract

In this paper we report on recent two-dimensional (2D) electron beam size measurements with a nonconventional synchrotron radiation interferometric technique based on x-ray heterodyne near field speckles (HNFS). The method relies on Fourier analysis of the random speckle patterns generated by a water suspension of nanospheres to assess the full 2D transverse coherence of the incoming x rays. The horizontal and vertical electron beam sizes are then retrieved by means of statistical optics approaches. The manuscript thoroughly describes the HNFS technique, and shows experimental results obtained at the ALBA Synchrotron Light Source. By changing the machine coupling, beam sizes as small as 5 μm are measured, thus improving on past measurements reported in the literature and proving the HNFS diagnostics suitable for low-emittance particle beams.

Accelerator Division
Alba Synchrotron Light Source
c/ de la Llum, 2-26
08290 Cerdanyola del Valles, Spain

Two-dimensional electron beam size measurements with x-ray heterodyne near field speckles

M. Siano,* B. Paroli, M. A. C. Potenza, and L. Teruzzi
Dipartimento di Fisica, Università degli Studi di Milano and INFN Sezione di Milano, via G. Celoria 16, 20133 Milan, Italy

U. Iriso, A. A. Nosych, E. Solano, and L. Torino
ALBA-CELLS Synchrotron Radiation Facility, Carrer de la Llum 2-26, 08290 Cerdanyola del Valles, Barcelona, Spain

D. Butti, A. Goetz, T. Lefevre, S. Mazzoni, and G. Trad
CERN, CH-1211 Geneva, Switzerland

(Received 20 December 2021; accepted 25 April 2022; published 9 May 2022)

In this paper we report on recent two-dimensional (2D) electron beam size measurements with a nonconventional synchrotron radiation interferometric technique based on x-ray heterodyne near field speckles (HNFS). The method relies on Fourier analysis of the random speckle patterns generated by a water suspension of nanospheres to assess the full 2D transverse coherence of the incoming x rays. The horizontal and vertical electron beam sizes are then retrieved by means of statistical optics approaches. The manuscript thoroughly describes the HNFS technique, and shows experimental results obtained at the ALBA Synchrotron Light Source. By changing the machine coupling, beam sizes as small as 5 μm are measured, thus improving on past measurements reported in the literature and proving the HNFS diagnostics suitable for low-emittance particle beams.

DOI: 10.1103/PhysRevAccelBeams.25.052801

I. INTRODUCTION

Two-dimensional (2D) beam size measurements are of fundamental importance to quantify the performance of current and future accelerators. Beam sizes, combined with the knowledge of the machine optical parameters, enable full characterization of the 2D emittance of electron beams [1,2]. Moreover, the transverse profile of electron beams determines the 2D spatial coherence properties of the emitted synchrotron radiation, thus directly impacting many research areas (such as physical sciences, biology and medicine, material sciences and archaeology, to name a few) that rely on coherence-based techniques [3].

Noninvasive beam size measurements exploiting the emitted synchrotron radiation are mainly performed via direct imaging or interferometry. Among direct imaging techniques, the x-ray pinhole camera is widely used at current third-generation light sources due to its simplicity [4,5]. It directly provides a 2D image of the source, though typically limited in resolution to beam sizes around 10 μm for 15 keV x rays [6]. The actual system resolution can be improved to a few micrometers by properly tailoring the source-to-pinhole and pinhole-to-detector distance, as well as by increasing the photon energy [6–8]. Interferometric beam size measurements based on the Young's double-slit scheme rely on the characterization of the spatial coherence of the emitted synchrotron light in the visible range [9,10]. Opposite to direct imaging, interferometric methods provide higher resolutions [11]. However, they are limited to one-dimensional (1D) measurements and can only probe two points at a time, thus making the full 2D coherence characterization lengthy [6]. Implementations with x rays also require challenging fabrication of high-quality apertures and x-ray optical components [12,13].

In this paper we describe full 2D beam size measurements with a nonconventional interferometric technique based on x-ray heterodyne near field speckles (HNFS). Originally conceived for particle sizing [14,15], the HNFS technique has recently found applications in coherence characterization of synchrotron radiation [16–20]. Here we show that the technique is intrinsically 2D and remarkably free of any dedicated x-ray optics. We report recent results obtained at the hard x-ray undulator beamline NCD-SWEET at the ALBA Synchrotron Light Source under different beam coupling conditions. We prove that the

*mirko.siano@unimi.it

method can resolve beam sizes as small as 5 μm with a relatively simple and compact (1-m-long) experimental setup.

The paper is organized as follows. In Sec. II we review the fundamentals of the HNFS technique. In Sec. III we describe the experimental setup installed at the NCD-SWEET beamline at the ALBA Synchrotron Light Source. In Sec. IV we present recent results obtained by changing the beam coupling in the storage ring. Finally, in Sec. V we draw our conclusions.

II. 2D COHERENCE MAPPING WITH HETERODYNE NEAR FIELD SPECKLES

The HNFS method relies on the scattering of the incoming x rays, produced by the electron beam, from a random ensemble of nanometric scatterers, in this case spherical nanoparticles suspended in water (a colloidal suspension). The self-referencing interference between the weak spherical waves scattered by the sample and the intense transilluminating x-ray beam generates a stochastic intensity distribution known as a speckle pattern. Fourier analysis of these speckle images allows direct 2D coherence mapping of the incoming x-ray beam [16,21]. The beam sizes along the two main axes of the electron beam can then be retrieved from the 2D coherence map by means of statistical optics approaches [22–24].

A. Single scatterer with a filament electron beam

We first consider the ideal case of a single scatterer located at the origin of a ξ-η plane at a distance Z_0 from the center of the synchrotron radiation source. The emitted x rays with wavelength λ impinge on the scatterer and the weak scattered spherical wave interferes with the intense transmitted photon beam. The resulting intensity is observed across a x-y plane at a distance z downstream the particle. The geometry of this so-called self-referencing interference is depicted in Fig. 1.

Adopting a common notation, in the following we will label scalar and vectorial quantities as x and $\vec{x}$, respectively. We will also deal with highly polarized radiation, as typically encountered in undulator sources [25], thus we will consider only the corresponding scalar component of the emitted electric field.

Let $e(\vec{x},z)$ denote the electric field of the x-ray synchrotron light across the observation plane and let $e_{s,\mathrm{ref}}(\vec{x},z)$ be the weak spherical wave scattered by the reference colloid, with $|e_{s,\mathrm{ref}}(\vec{x},z)| \ll |e(\vec{x},z)|$. They can both be related to the incident field across the scattering plane $e(\vec{x},z=0)$ [21]:

$$\begin{aligned} e(\vec{x},z) &= e(\vec{x},z=0)e^{ikz} \\ e_{s,\mathrm{ref}}(\vec{x},z) &= e(\vec{x}_{\mathrm{ref}},z=0)\frac{s(0)}{kz}e^{ikz}e^{ik\frac{\Delta r^2}{2z}}, \end{aligned} \tag{1}$$

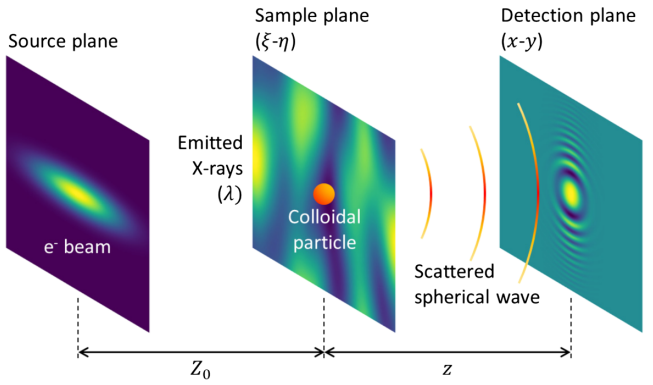

FIG. 1. Geometry for the self-referencing interference between the intense transilluminating x-ray beam and the weak scattered spherical wave. The case of interest in this paper of a horizontally elongated electron beam is depicted. From left to right: 2D electron beam distribution at the source plane, time-resolved field distribution of the emitted x rays impinging onto the scatterer, and finally time-integrated single-scatterer interference pattern.

where $k = 2\pi/\lambda$, $\vec{x}_{\mathrm{ref}}$ is the projection onto the x-y plane of the transverse position of the reference colloid, $s(0)$ is the amplitude of the scattered wave in the forward direction [26] and $\Delta r = |\Delta\vec{x}| = |\vec{x} - \vec{x}_{\mathrm{ref}}|$.

In the following, we understand the explicit dependence on $z = 0$ and simply write $e(\vec{x})$ to describe the electric field of the incoming synchrotron light across the scattering plane. We work under the conditions of a slowly varying intensity distribution of the incoming x rays, as is typical in third-generation synchrotron light sources. By this we mean that the intensity distribution of the emitted x rays varies appreciably over a characteristic length scale much larger than the transverse extension of the coherence areas σ_{coh}. Since we are interested in the characterization of the spatial coherence properties of the emitted synchrotron light, in the following we treat the intensity distribution of the incoming x rays as uniform for notation simplicity, in such a way that $|e(\vec{x})|^2 = |e(\vec{x}_{\mathrm{ref}})|^2 = i_0$ over spatial scales comparable to σ_{coh}. In Sec. IV we will show that the same formalism developed hereafter can be applied also in the presence of intensity modulations, even if irregular, as long as they are stationary. Finally, $\vec{x}_{\mathrm{ref}} = (0,0)$ throughout the paper.

A filament (i.e., zero-emittance) electron beam acts as a pointlike source. In this case, the emitted synchrotron light is fully coherent. The intensity distribution $i(\vec{x},z)$ resulting from the interference between the transmitted x-ray beam and the weak scattered spherical wave is therefore given by

$$\begin{aligned} i(\vec{x},z) &= |e(\vec{x},z) + e_{s,\mathrm{ref}}(\vec{x},z)|^2 \\ &\approx |e(\vec{x})|^2 + 2\Re\{e(\vec{x},z)e^*_{s,\mathrm{ref}}(\vec{x},z)\} \\ &= i_0\left[1 + 2\frac{s(0)}{kz}i_{\mathrm{ref}}(\vec{x},z)\right], \end{aligned} \tag{2}$$

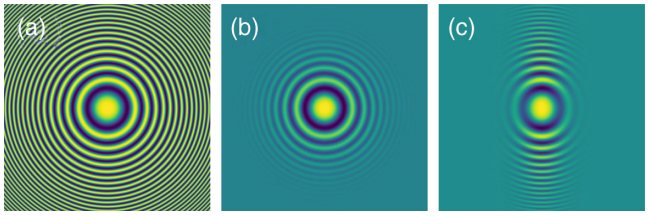

FIG. 2. Simulated single-scatterer interference pattern in the case of a filament electron beam (a), a round electron beam (b) and a horizontally elongated electron beam (c). Plots refer to Eqs. (3) and (6), namely the interference pattern generated by a single scatterer on top of the (uniform) x-ray intensity distribution. The side of each square is 140 μm. Simulation parameters: $\lambda = 0.1$ nm, $Z_0 = 30$ m, $z = 2$ m, 23 μm (H) $\times$ 23 μm (V) electron beam in (b), 45 μm (H) $\times$ 11 μm (V) electron beam in (c).

where

$$i_{\mathrm{ref}}(\vec{x}, z) = \cos\left(\frac{k\Delta r^2}{2z}\right) \tag{3}$$

describes the intensity modulations on top of i_0 due to the single-scatterer interference fringes. Due to the peculiar interference between the incoming beam and the scattered spherical wave, the interference fringes described in Eq. (3) are circular, as shown in Fig. 2(a). Their spatial frequency progressively increases with $\Delta\vec{x}$. This allows to introduce a one-to-one relation, known as the spatial scaling, which maps spatial frequencies $\vec{q}$ into transverse displacements $\Delta\vec{x}$ [16,21]:

$$\Delta\vec{x} = z\frac{\vec{q}}{k}. \tag{4}$$

B. Single scatterer with a finite emittance electron beam

Opposite to the case of a pointlike source, an electron beam with finite emittance generates synchrotron light endowed with partial coherence. Under quasimonochromatic conditions [22–24], the emitted radiation is fully temporally coherent and we can neglect temporal coherence effects [20]. The transverse coherence properties of the incoming x-ray wave front at the scattering plane are therefore described by the normalized two-point correlation function known in statistical optics as the 2D complex coherence function (CCF) [22–24]:

$$\mu(\vec{x}_2 - \vec{x}_1) = \frac{\langle e(\vec{x}_1)e^*(\vec{x}_2)\rangle}{\sqrt{\langle|e(\vec{x}_1)|^2\rangle\langle|e(\vec{x}_2)|^2\rangle}}, \tag{5}$$

where $\vec{x}_1$ and $\vec{x}_2$ are two points on the wave front of the synchrotron radiation and $\langle\cdot\rangle$ denotes ensemble average over many statistical realizations of the electric field distribution.

In general, the limited transverse coherence of a light wave cancels high-frequency interference fringes [22–24]. In the particular case of the single-scatterer interference pattern, this implies that Eq. (3) is modified as follows:

$$i_{\mathrm{ref}}(\vec{x}, z) = |\mu(\Delta\vec{x})| \cdot \cos\left(\frac{k\Delta r^2}{2z}\right). \tag{6}$$

Notice that in the fully coherent case $|\mu(\Delta\vec{x})| = 1$ and Eq. (6) reduces to Eq. (3). Examples of the resulting interference pattern generated by a single scatterer on top of the (uniform) x-ray intensity distribution are shown in Figs. 2(b) and 2(c) for the cases of a round electron beam and of a horizontally elongated electron beam, respectively. In both cases, the outermost fringes vanish, while the innermost remain [16,21]. This shows how coherence works, being the ability of the radiation of generating stable interference fringes [22–24]. On the other way around, the visibility of the interference fringes from a single scatterer allows to directly assess the 2D coherence properties of the incoming radiation at the scattering plane. In particular, many interference fringes with high spatial frequency appear along the direction of larger coherence, i.e., where the beam size is smaller.

C. Colloidal suspension with a finite emittance electron beam

With a colloidal suspension composed by many scatterers, the observed intensity distribution is a random speckle field, in contrast with the well-defined interference pattern generated by a single colloid. To formally describe the intensity distribution across the x-y plane, we assume heterodyne conditions [14]:

$$|e_s(\vec{x}, z)| \ll |e(\vec{x}, z)|, \tag{7}$$

where $e_s(\vec{x}, z) = \sum e_{s,j}(\vec{x}, z)$ is the total electric field scattered by the suspension, given by the sum of the individual spherical waves $e_{s,j}(\vec{x}, z)$ scattered by each colloid. Under heterodyne conditions, the scattered field is typically a few percent of the incoming beam, in such a way that $|e_s(\vec{x}, z)|/|e(\vec{x}, z)| < 0.1$. It can be shown that heterodyne conditions are equivalent to the single-scattering regime [26]. In practice, this implies that heterodyne conditions are fulfilled at x-ray wavelengths by properly diluting the sample to volume concentrations of the order of 10% or lower.

Under heterodyne conditions, the total intensity distribution can be approximated as follows [16,21]:

$$\begin{aligned} i(\vec{x}, z) &= |e(\vec{x}, z) + e_s(\vec{x}, z)|^2 \\ &\approx i_0 + 2\Re\{e(\vec{x}, z)e_s^*(\vec{x}, z)\}, \end{aligned} \tag{8}$$

where i_0 represents the intensity of the incoming beam, $i_{\mathrm{het}}(\vec{x}, z) = \Re\{e(\vec{x}, z)e_s^*(\vec{x}, z)\}$ is the so-called heterodyne

term describing the observed speckles and we neglect the so-called homodyne term $|e_s(\vec{x},z)|^2$ describing the mutual interference between the spherical waves scattered by different colloids. Equation (8) is valid with an accuracy $|e_s(\vec{x},z)|/2|e(\vec{x},z)|$ of a few percent.

By expanding the scattered field $e_s(\vec{x},z)$ and exploiting Eqs. (2) and (6), the heterodyne term takes the following form:

$$\begin{aligned} i_{\mathrm{het}}(\vec{x},z) &= \Re\left\{ e(\vec{x},z)\sum_{j=1}^{N} e^*_{s,j}(\vec{x},z)\right\} \\ &= \sum_{j=1}^{N} \Re\{e(\vec{x},z)e^*_{s,j}(\vec{x},z)\} \\ &= i_0\frac{s(0)}{kz}\sum_{j=1}^{N} i_{\mathrm{ref}}(\vec{x},z)\otimes\delta(\vec{x}-\vec{x}_j), \end{aligned} \tag{9}$$

where $\vec{x}_j$ represents the projection onto the x-y plane of the transverse position of the jth scatterer and $\otimes$ denotes a convolution product.

Equation (9) shows that heterodyne speckles arise from the intensity sum of many equal single-scatterer interference patterns $i_{\mathrm{ref}}(\vec{x},z)$ described by Eq. (6) and generated by colloids randomly positioned within the suspension. As a consequence, the power spectrum of heterodyne speckles $I(\vec{q},z)$ is proportional to the power spectrum of the single-scatterer interference pattern $I_{\mathrm{ref}}(\vec{q},z)$, as also shown in Fig. 3:

$$\begin{aligned} I(\vec{q},z) &= \left| FT\left\{\sum_{j=1}^{N} i_{\mathrm{ref}}(\vec{x},z)\otimes\delta(\vec{x}-\vec{x}_j)\right\}(\vec{q})\right|^2 \\ &= |FT\{i_{\mathrm{ref}}(\vec{x},z)\}|^2\cdot\left|\sum_{j=1}^{N} e^{i\vec{q}\cdot\vec{x}_j}\right|^2 \\ &= NI_{\mathrm{ref}}(\vec{q},z), \end{aligned} \tag{10}$$

where in the second line the linearity and the convolution theorem of the Fourier transform operation have been used [27], while in the last line $|\sum\exp(i\vec{q}\cdot\vec{x}_j)| = \sqrt{N}$ is the limit of the random phasor sum for $N \gg 1$ [22–24]. We recall that, under heterodyne conditions, the homodyne term $|e_s(\vec{x},z)|^2$ is a few percent of the heterodyne term $\Re\{e(\vec{x},z)e^*_s(\vec{x},z)\}$. Therefore, neglecting the homodyne contribution to the power spectrum in Eq. (10) can be done with an accuracy of at least 1% due to the square in the Fourier transform operation.

The Fourier transform in the last line of Eq. (10), namely the Fourier transform of the single-scatterer interference pattern described in Eq. (6), is rigorously a convolution integral. It reduces to a simple product under the so-called near-field conditions [16,21] and Eq. (10) takes the following form:

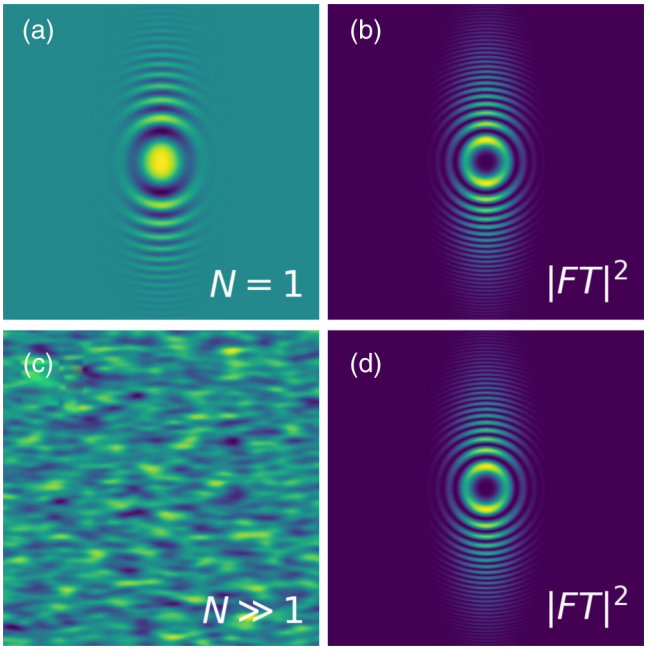

FIG. 3. Simulated single-scatterer interference pattern (a) and corresponding 2D power spectrum (b) for a horizontally elongated electron beam. Simulated heterodyne speckles (c) and corresponding 2D power spectrum (d) for the same electron beam configuration as in (a) and (b). Notice that the power spectrum of heterodyne speckles closely resembles the power spectrum of the single-scatterer interferogram.

$$I(\vec{q},z) = N\left|\mu\left(z\frac{\vec{q}}{k}\right)\right|^2 T(q,z), \tag{11}$$

where

$$T(q,z) = 2\sin^2\left(\frac{zq^2}{2k}\right) \tag{12}$$

and $q = |\vec{q}|$.

Equation (11) shows that the power spectrum of heterodyne speckles exhibits peculiar oscillations known as Talbot oscillations, enveloped by the squared modulus of the 2D CCF of the incoming synchrotron light at the scattering plane. We stress that the power spectrum of heterodyne speckles closely resembles the power spectrum of the single-scatterer interferogram. Therefore, although heterodyne speckles appear as a random pattern in the direct space, coherence information is preserved in the Fourier space, as evidenced in Fig. 3. Notice that in Eq. (11) the same spatial scaling as in Eq. (4) allows to effectively map spatial frequencies (Fourier-space coordinates) into transverse displacements (direct-space coordinates). This enables direct 2D coherence mapping.

A summary of the technique is provided in Fig. 4 for three different electron beam configurations of interest in the accelerator community.

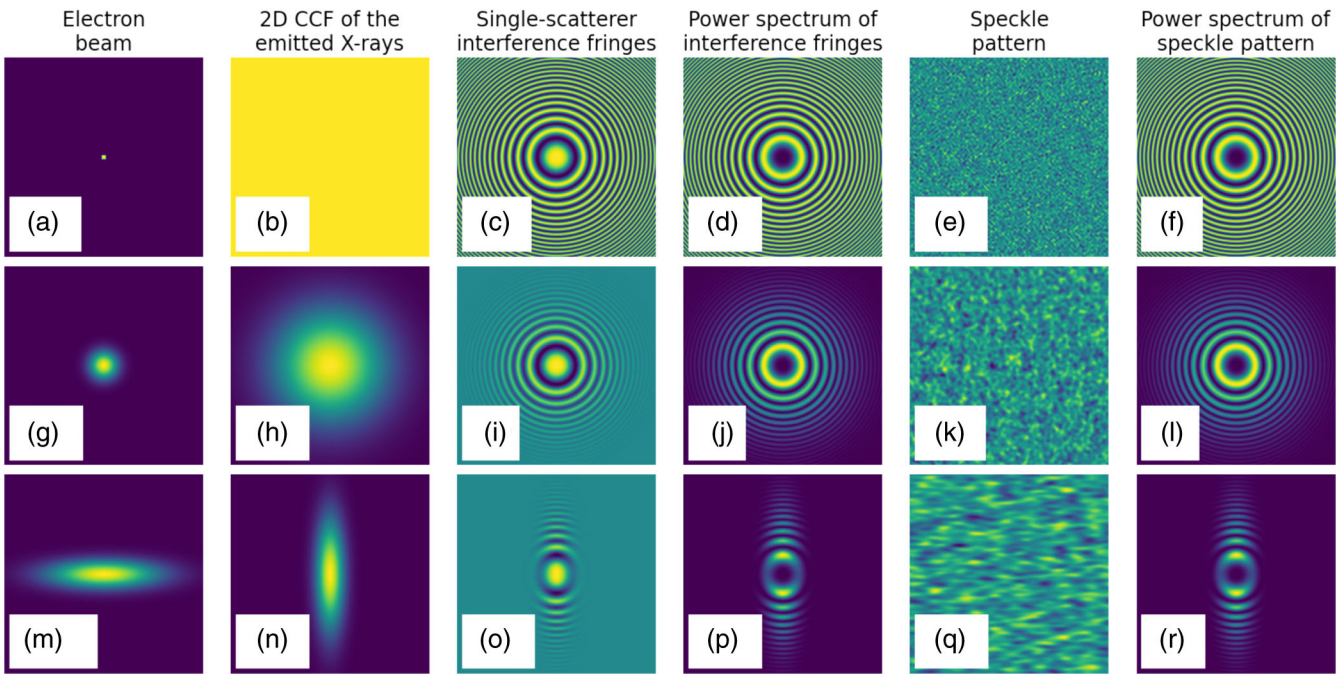

FIG. 4. Summary of the HNFS technique showing the relation between the 2D profile of the electron beam [(a), (g), and (m)], the modulus of the 2D CCF $\mu(\Delta\vec{x})$ of the emitted synchrotron radiation [(b), (h), and (n)], the single-scatterer interference fringes $i_{\mathrm{ref}}(\vec{x}, z)$ [(c), (i), and (o)] and the corresponding 2D power spectrum $I_{\mathrm{ref}}(\vec{q}, z)$ [(d), (j), and (p)], the heterodyne speckle pattern $i_{\mathrm{het}}(\vec{x}, z)$ generated by a large number of scatterers [(e), (k), and (q)] and finally the 2D power spectrum of heterodyne speckles $I(\vec{q}, z)$ [(f), (l), and (r)]. The case of a filament electron beam [(a), (b), (c), (d), (e), and (f)], a round electron beam [(g), (h), (i), (j), (k), and (l)] and a horizontally elongated electron beam [(m), (n), (o), (p), (q), and (r)] are depicted. Notice the relation between the 2D transverse profile of the electron beam, the 2D CCF of the emitted synchrotron light and the envelope of the Talbot oscillations in the 2D power spectrum.

D. The effective Talbot transfer function

The Talbot transfer function in Eq. (12) is strictly valid for a pure 2D sample with null thickness and for an infinite detection plane [21]. Remarkably, deviations from these assumptions can still be described analytically.

Scattering from a 3D sample with thickness t modifies the Talbot oscillations as follows [28]:

$$T_{3D}(q,z) = \frac{1}{t}\int_{z-t/2}^{z+t/2} T(q,z')\mathrm{d}z' = 1-\cos\left(\frac{zq^2}{k}\right)\mathrm{sinc}\left(\frac{tq^2}{2k}\right). \quad (13)$$

A finite detection screen with lateral size L induces a tapering of the Talbot oscillations for increasing q (walk-off effect) [29]:

$$T_{wo}(q,z) = \begin{cases} 1+\beta(q,z)[T(q,z)-1] & q \le kL/(2z) \\ 1 & q > kL/(2z) \end{cases}$$
$$\beta(q,z) = \frac{L-2zq/k}{L+2zq/k}. \quad (14)$$

By combining Eqs. (13) and (14), the most general case where both effects are simultaneously present is described by the following transfer function:

$$T_{\mathrm{eff}}(q,z) = \frac{1}{t}\int_{z-t/2}^{z+t/2} T_{wo}(q,z')\mathrm{d}z'. \quad (15)$$

The solution of Eq. (15) is generally obtained with numerical methods. In Fig. 5 we compare both $T_{3D}(q,z)$ and $T_{wo}(q,z)$ against $T(q,z)$ for the actual experimental parameters described in Sec. III. The comparison evidences that Talbot oscillations are mainly affected by the walk-off effect, whereas the 3D effect is negligible with the parameters of interest here, and Eq. (15) reduces to Eq. (14) in this case.

E. General formulation of the HNFS technique

In practice, other contributions that were not considered in the previous formulation affect the envelope of the Talbot oscillations.

The finite resolution of the detection system blurs high-frequency interference fringes, which eventually vanish. This is described in the direct space by the convolution of Eq. (9) with the point-spread function of the detection system, and in the Fourier space by the multiplication of Eq. (11) with the modulation transfer function $H(\vec{q})$ of the detection system [27].

In addition, colloids do not scatter light isotropically [26]. As a result, the Talbot oscillations are modulated by

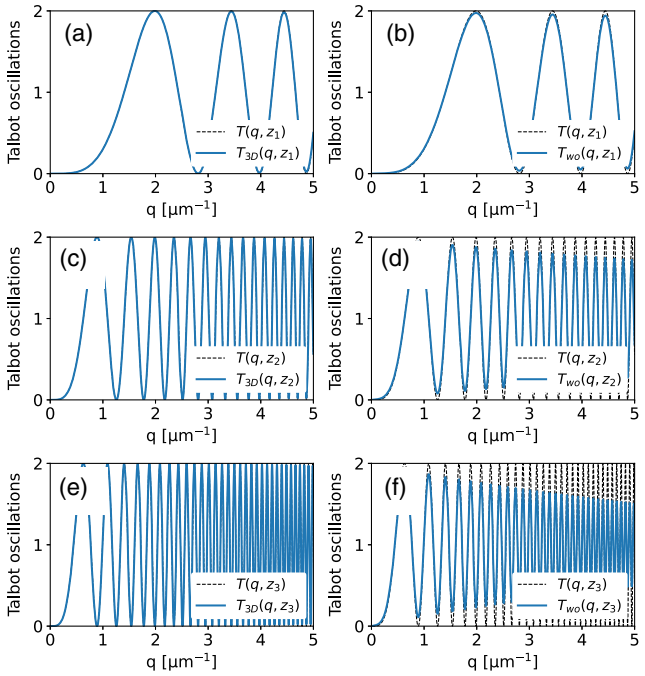

FIG. 5. Effect of 3D scattering [(a), (c), and (e)] and walk-off [(b), (d), and (f)] on Talbot oscillations for three progressively increasing sample-detector distances $z_1 = 5$ cm [(a) and (b)], $z_2 = 25$ cm [(c) and (d)] and $z_3 = 50$ cm [(e) and (f)] and for the actual experimental parameters described in Sec. III.

the particle form factor $S(\vec{q})$ which represents the relative strength of the intensity scattered along the wave vector $\vec{q}$ [15].

Finally, an additive term $P(\vec{q})$ is introduced to account for any noise contribution, mainly shot noise and readout noise.

Equation (11) is therefore generalized as follows [16,21]:

$$I(\vec{q}, z) = T_{\text{eff}}(q, z)\left|\mu\left(z\frac{\vec{q}}{k}\right)\right|^2 H(\vec{q})S(\vec{q}) + P(\vec{q}). \quad (16)$$

F. The importance of the spatial scaling

The spatial scaling of Eq. (4) enables direct 2D coherence measurements by mapping Fourier-space coordinates into transverse displacements. We also notice that the walk-off effect has a unique representation in terms of direct space coordinates since Eq. (14) exhibits the same spatial scaling as in Eq. (4). As a consequence, data acquired at different sample-detector distances can be consistently compared upon the spatial scaling and the envelopes of the Talbot oscillations are described by

$$\begin{aligned} \text{upper} &\rightarrow u(\Delta x^i) = [1 + \beta(\Delta x^i)]|\mu(\Delta x^i)|^2 \\ \text{lower} &\rightarrow w(\Delta x^i) = [1 - \beta(\Delta x^i)]|\mu(\Delta x^i)|^2, \end{aligned} \quad (17)$$

where either $\Delta x^i = \Delta x$ or $\Delta x^i = \Delta y$ along the horizontal or vertical direction, respectively. An example of the upper and lower envelope along the horizontal direction is shown in Fig. 6.

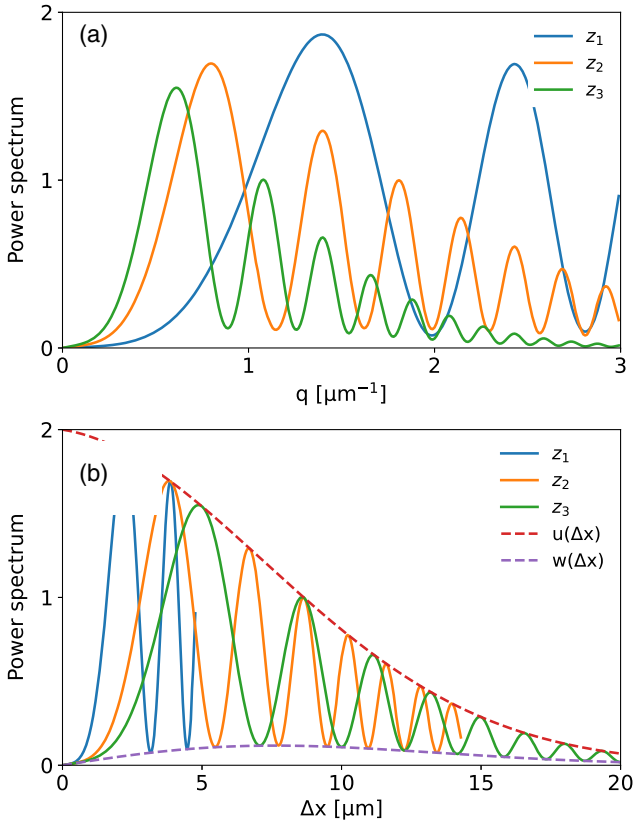

FIG. 6. Simulated horizontal profiles of 2D power spectra for three different distances $z_1 = 10$ cm, $z_2 = 30$ cm and $z_3 = 50$ cm as a function of Fourier wave vectors (a) and transverse displacements (b). Upon the spatial scaling, Talbot maxima and minima clearly fit onto the two unique master curves of the upper and lower envelope $u(\Delta x)$ and $w(\Delta x)$, respectively, as described by Eq. (17).

G. Effects of limited temporal coherence on source size measurements

In general, the limited temporal coherence of the emitted synchrotron light might contribute to the loss of visibility of the interference fringes from a single scatterer. This would imply an additional decay of the Talbot oscillations in the power spectrum of heterodyne speckles from a colloidal suspension [19–21]:

$$\begin{aligned} I(\vec{q}, z) = T_{\text{eff}}(q, z)\left|\mu\left(z\frac{\vec{q}}{k}\right)\right|^2 \cdot \left|\gamma\left(\frac{zq^2}{2ck^2}\right)\right|^2 \\ \times H(\vec{q})S(\vec{q}) + P(\vec{q}), \end{aligned} \quad (18)$$

where c is the speed of light and $\gamma(\Delta t) = \gamma(t_2 - t_1) = \langle e(t_1)e^*(t_2)\rangle / \sqrt{\langle|e(t_1)|^2\rangle\langle|e(t_2)|^2\rangle}$ describes the temporal coherence of the emitted synchrotron light and is known in statistical optics as the complex degree of self-coherence

(CDC) [22–24]. It would result in an increased source size if not properly accounted for. However, Eq. (18) also shows that spatial and temporal coherence effects can actually be disentangled, thus independently characterized, from the superposition of data at different z upon either the spatial scaling $\Delta\vec{x} = z\vec{q}/k$ (spatial master curve criterion) or the temporal scaling $\Delta t = zq^2/2ck^2$ (temporal master curve criterion), respectively [19–21]. For the case of interest here, radiation is quasimonochromatic, as we will detail in Sec. III, and $\gamma(\Delta t) = 1$ in Eq. (18), thus temporal coherence effects are negligible.

III. HNFS SETUP AT THE NCD-SWEET BEAMLINE (ALBA)

We applied the HNFS method to perform 2D electron beam size measurements at the hard x-ray undulator beamline NCD-SWEET of the ALBA Synchrotron Light Source. The experimental setup is sketched in Fig. 7 and the main parameters are summarized in Table I.

The radiation source is an in-vacuum undulator with a number of periods $N_w = 92$ and period length $\lambda_w = 21.6$ mm. X rays are generated by the electron beam with nominal energy $E = 2.98$ GeV. A Si(111) channel-cut monochromator selects the radiation wavelength $\lambda = 0.1$ nm, corresponding to the 7th harmonic of the undulator, providing a quasimonochromatic beam with a relative bandwidth $\Delta\lambda/\lambda \sim 10^{-4}$. The x rays impinge onto a water suspension of silica spheres with diameter $d = 500$ nm, stored in 2-mm-thick capillaries at a distance $Z_0 = 33$ m from the undulator center. The volume concentration of the sample is roughly 10%, which ensures heterodyne conditions. One additional capillary filled with distilled water is used to characterize the noise contribution $P(\vec{q})$. Speckles are recorded at distances z ranging from 2 cm up to 1.2 m downstream the sample. A YAG:Ce scintillator screen with thickness 50 μm is used to convert x-ray photons into visible light. A microscope objective with nominal magnification 20x projects the visible light onto the sensor (Basler acA4112–8 gm with 3.45 μm pixel size). A 45-deg mirror is inserted between the scintillator

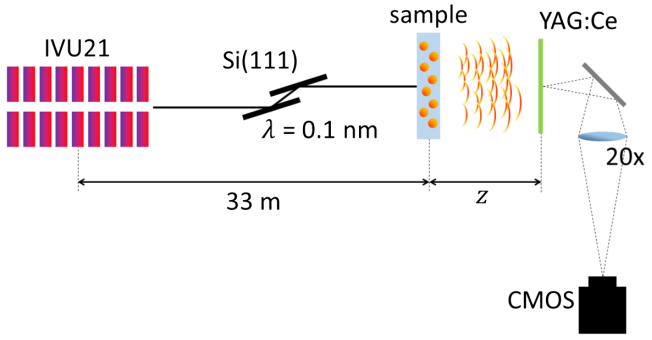

FIG. 7. HNFS experimental setup at the NCD-SWEET beamline at ALBA.

TABLE I. Main parameters of the HNFS setup installed at the NCD-SWEET beamline at ALBA.

Parameter	Symbol	Value
Electron beam energy	E	2.98 GeV
Undulator number of periods	N_w	92
Undulator period length	λ_w	21.6 mm
Radiation wavelength	λ	0.1 nm
Monochromator bandwidth	$\Delta\lambda/\lambda$	10^{-4}
Undulator harmonic		7th
Flux at sample position		1.5×10^{12} ph/s
Material of scatterers		SiO_2
Diameter of scatterers	d	500 nm
Volume concentration		10%
Distance from undulator center	Z_0	33 m
Sample-detector distance	z	2 cm–1.2 m
Camera		Basler
Camera model		acA4112–8 gm
Sensor type		CMOS
Bit depth		12 bit
Pixel size	d_{pxl}	3.45 μm
Exposure time	ET	50 ms
Frame rate		1 Hz

and the optics to prevent the transmitted x rays from damaging the lenses and the sensor. For each z, we acquire a stack of 50 images to increase statistics. Exposure time is fixed at 50 ms. The acquisition frame rate is set to 1 Hz in such a way that consecutive speckle images are statistically independent due the random motions of the sample.

To test the sensitivity of the technique, we change the vertical beam size at the NCD source point by varying the vertical emittance ϵ_y of the electron beam. In synchrotron light sources like ALBA, ϵ_y is much smaller than the horizontal emittance ϵ_x and it is given by the coupled motions between the horizontal and vertical planes [30,31]. In these cases, we can approximate the coupling factor κ of the electron beam by $\kappa = \epsilon_y/\epsilon_x$ [30]. We can vary the vertical emittance by using different settings of the skew quadrupoles, which transfer the betatron motion between the horizontal and vertical planes, thereby controlling the coupling factor within a certain range. For these experiments, the coupling factors were $\kappa = [0.5, 0.65, 1.6, 2.8]\%$, and they were inferred from the emittances measured with the x-ray pinhole camera at FE34 (in operation since 2011 [32]).

IV. EXPERIMENTAL RESULTS AND DISCUSSION

An example of acquisition is reported in Fig. 8(a). It shows tiny faint speckles on top of large-scale intensity modulations. The latter are observed also by removing the sample and are therefore produced by some imperfections of the beamline components. Also notice the presence of stray-light contributions due to dust particles on the YAG

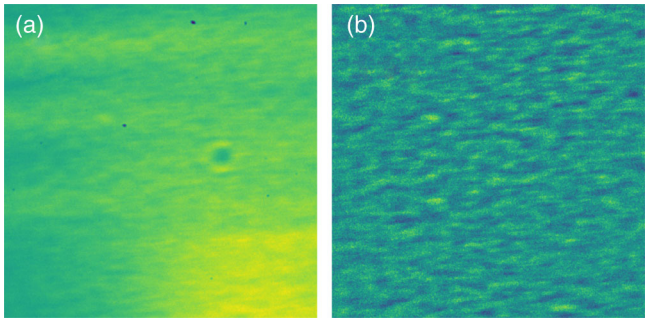

FIG. 8. Acquired raw data (a) and corresponding differential heterodyne speckles resulting from the DFA (b). Notice that the speckle pattern is remarkably uniform, despite the intensity modulations and stray-light contributions clearly visible in the raw image. The side of each square image is roughly 260 μm in real space. Data refer to $\kappa = 0.50\%$ and $z = 1.1$ m.

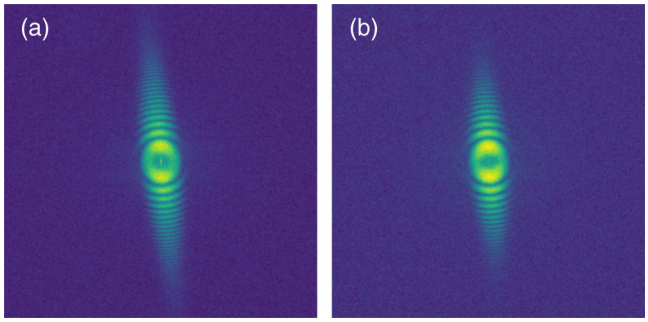

FIG. 9. 2D power spectra at $\kappa = 0.50\%$ (a) and $\kappa = 2.80\%$ (b). Data refer to $z = 1.1$ m.

(the big circles at the center of the image) and on the camera sensor (the small black dots throughout the image). Such intensity modulations and disturbances are stationary, opposite to the case of speckles. Thus the genuine speckle pattern is extracted from the static background by means of a differential analysis of consecutive images [double frame analysis (DFA)] [14]:

$$s_{j,l}(\vec{x}, z) = \frac{i_j(\vec{x}, z) - i_{j+l}(\vec{x}, z)}{i_j(\vec{x}, z) + i_{j+l}(\vec{x}, z)}, \tag{19}$$

where $s_{j,l}(\vec{x}, z)$ is the differential speckle signal, $i_j(\vec{x}, z)$ and $i_{j+l}(\vec{x}, z)$ are two different images described by Eq. (8) with index j and $j + l$, respectively, from the same acquisition stack. In the following, we will adopt $l = 1$. The result of the DFA is shown in Fig. 8(b). Speckles are remarkably uniform, as if the intensity distribution of the incoming x rays was constant. This experimentally proves that the DFA is effective in reducing stationary intensity modulations and stray-light contributions, which ultimately do not affect measurements. Therefore, the formalism developed in Sec. II can be applied.

For each $s_{j,l=1}(\vec{x}, z)$ we compute the corresponding power spectrum $I_{j,l=1}(\vec{q}, z) = |FT\{s_{j,l=1}(\vec{x}, z)\}(\vec{q})|^2$ and we average the results to increase statistics:

$$I(\vec{q}, z) = \frac{1}{N-1} \sum_{j=1}^{N-1} I_{j,l=1}(\vec{q}, z). \tag{20}$$

Examples of power spectra acquired at the same sample-detector distance $z = 1.1$ m for $\kappa = 0.50\%$ and $\kappa = 2.80\%$ are reported in Fig. 9.

Power spectra are rotated by roughly 5 degrees with respect to the nominal vertical direction due to a relative tilt between the actual beam axes and the sensor orientation. Regardless of such misalignments, the actual horizontal and vertical axes of the electron beam can be unambiguously identified. Furthermore, since the overall rotation of the 2D power spectra is unchanged, the coupling scan does not appreciably change the beam tilt at the undulator location.

A qualitative analysis of the 2D power spectra allows to extract useful information. Power spectra are elongated along the vertical direction, in a clear indication that the vertical beam size is much smaller than the horizontal one. Furthermore, the horizontal width of the power spectra is roughly the same for all couplings, whereas the vertical elongation of the power spectra progressively decreases. This is particularly evident by comparing the power spectra shown in Fig. 9. This suggests that the horizontal beam size is unchanged during the coupling scan, whereas the vertical beam size increases with the coupling.

Quantitatively, data analysis is based on Eq. (16) according to the following procedure. We first extract horizontal and vertical profiles separately and we measure the noise baseline $P(q)$ from the power spectrum of the capillary filled with water. We then characterize the product $H(q)S(q)$, which we refer to as the calibration function, by performing measurements close enough to the scattering sample:

$$H(q)S(q) = \frac{I(q, z)_{z\to 0} - P(q)}{T_{\text{eff}}(q, z)}. \tag{21}$$

Equation (21) directly derives from Eq. (16) in the limit $z \to 0$, since $|\mu(zq/k)|^2 \to |\mu(0)|^2$ thanks to the spatial scaling and $|\mu(0)| = 1$ from the definition in Eq. (5). We perform a piecewise analysis to avoid division by the Talbot minima in Eq. (21) and we combine data from a few different positions to fill in the gaps by taking advantage of the fact that Talbot oscillations change by varying the distance. We stress that these operations ensure that the calibration function is measured under the actual working conditions of the experiment.

We then use the measured $P(q)$ and $H(q)S(q)$ to extract the coherence properties of the incoming radiation from Eq. (16):

$$T_{\mathrm{eff}}(q,z)\left|\mu\left(z\frac{q}{k}\right)\right|^2=\frac{I(q,z)-P(q)}{H(q)S(q)}. \tag{22}$$

It is here worth mentioning that the unavoidable motions of the scatterers during the exposure time blur the speckle patterns. This results in a further decay of the Talbot oscillations and the power spectra are, in principle, exposure dependent. However, these contributions are automatically accounted for in the calibration function if all acquisitions are performed with the same exposure time and the statistical properties of the sample dynamics do not vary in time. This was verified by periodically monitoring the calibration curve during the experiment. Therefore, data reduction based on Eqs. (21) and (22) enables effective and rigorous compensation of the scatterer motions in real-case scenarios, regardless of the origin of the sample dynamics (whether diffusive or convective). Alternatively, speckles can also be generated by static membranes [15,18].

Upon the processing procedure of Eqs. (21) and (22), we merge data from different distances by exploiting the spatial scaling. An example is reported in Fig. 10 for the beam coupling $\kappa = 2.80\%$. Scaled Talbot maxima and minima fit onto two unique master curves that can be fitted according to Eq. (17) by assuming a Gaussian CCF:

$$\begin{aligned} u(\Delta x^i) &= [1+\beta(\Delta x^i)]\cdot|\exp[-(\Delta x^i)^2/2\sigma^i_{\mathrm{coh}}]|^2 \\ w(\Delta x^i) &= [1-\beta(\Delta x^i)]\cdot|\exp[-(\Delta x^i)^2/2\sigma^i_{\mathrm{coh}}]|^2, \end{aligned} \tag{23}$$

where either $\Delta x^i = \Delta x$ and $\sigma^i_{\mathrm{coh}} = \sigma^H_{\mathrm{coh}}$ along the horizontal direction, or $\Delta x^i = \Delta y$ and $\sigma^i_{\mathrm{coh}} = \sigma^V_{\mathrm{coh}}$ along the vertical one. The rms widths of the Gaussian CCF σ^H_{coh} and σ^V_{coh} are known as the horizontal and vertical transverse coherence length of the incoming synchrotron radiation, respectively. They are the only free parameters in the entire data reduction procedure, which makes the HNFS technique fully self-consistent for what concerns coherence characterization of the incoming x-ray beam.

From the measured horizontal and vertical coherence lengths $\sigma^{H,V}_{\mathrm{coh}}$, a theoretical model is needed to retrieve the corresponding electron beam size. In this framework, the classical approach adopts the well-known Van Cittert and Zernike theorem [22–24]:

$$\sigma^{H,V}_{\mathrm{beam,VCZ}} = \frac{\lambda Z_0}{2\pi\sigma^{H,V}_{\mathrm{coh}}}. \tag{24}$$

However, the Van Cittert and Zernike theorem is strictly valid for incoherent radiation sources [22–24] and its applicability to third-generation synchrotron light sources is debated [33,34]. Therefore, we propose a second model to map the 2D x-ray coherence into the corresponding electron beam sizes. The method relies on precomputed look-up tables (LUTs) obtained via extensive simulations following the formulas in [33,35]. We label the corresponding horizontal and vertical beam sizes as $\sigma^{H,V}_{\mathrm{beam,LUT}}$.

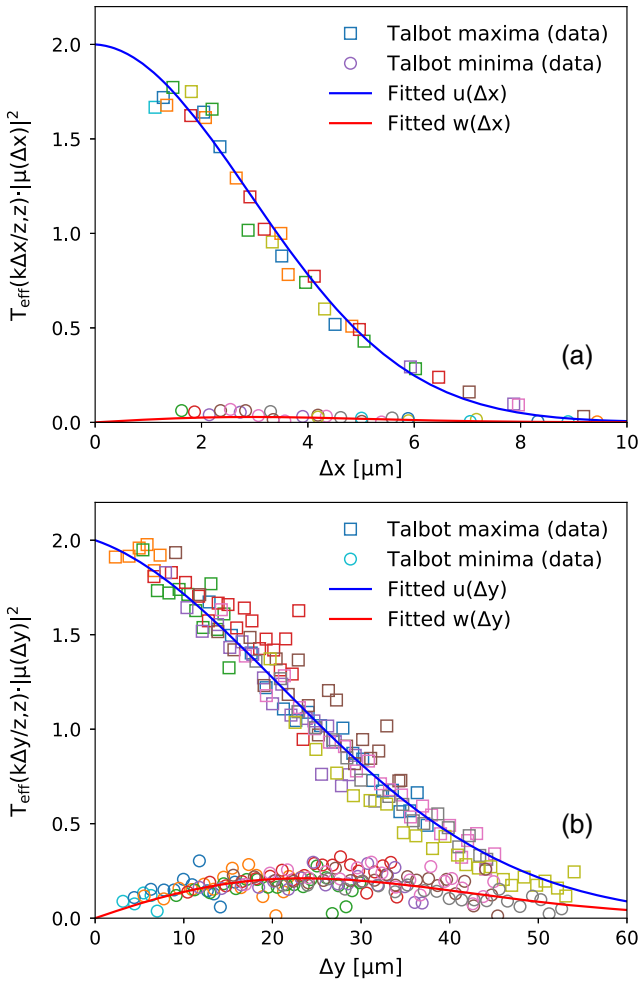

FIG. 10. Master curves describing the upper and lower envelopes of Talbot oscillations along the horizontal (a) and vertical (b) direction for $\kappa = 2.80\%$. Different colors represent different sample-detector distances z.

We prefer to follow the latter formalism, as it accounts for more realistic conditions like deviations from a perfectly incoherent radiation source, the finite energy spread of the particle beam ($\Delta E/E = 1.05\times10^{-3}$) and small detunings in the radiation wavelength, as already shown in previous publications [16,36]. The proposed approach has been validated with SRW (Synchrotron Radiation Workshop) simulations [37,38]. Its limitations and range of applicability stem from the ultrarelativistic approximation and the free-space propagation of the x-ray beam. The case of an imaging configuration with lenses or focusing mirrors (without surface errors) can also be treated by this method upon a proper scaling of distances and by including the correct magnification factor [16,34].

Results are reported in Fig. 11 and are summarized in Table II. Expected values $\sigma^{H,V}_{\mathrm{beam,th}}$ are derived by combining beam size measurements from the x-ray pinhole camera at FE34 and LOCO (Linear Optics from Closed Orbit) measurements [39–41] of the machine optical parameters at the operational coupling $\kappa = 0.65\%$. The reference

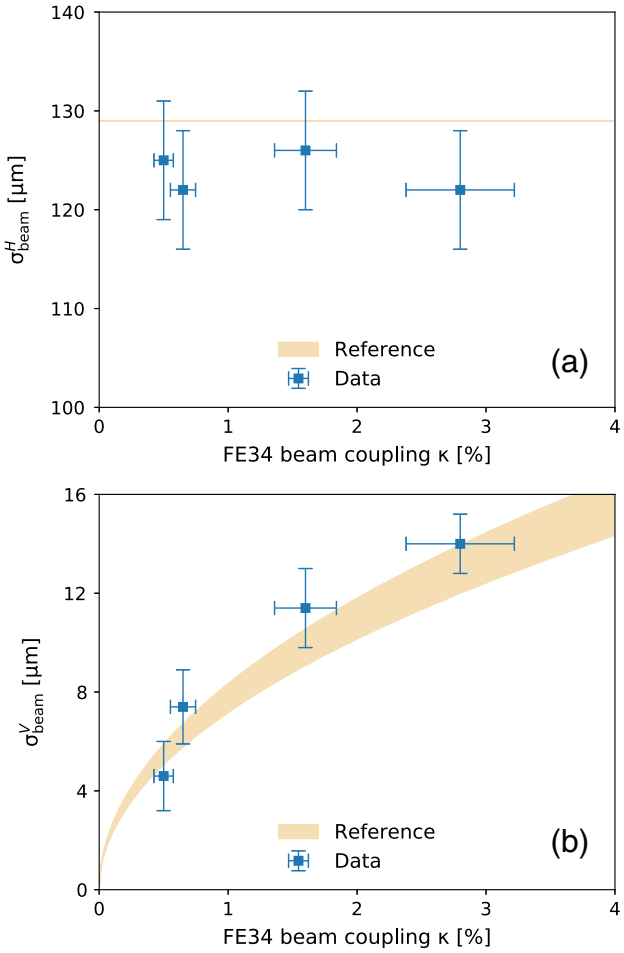

FIG. 11. Measured horizontal (a) and vertical (b) beam sizes as a function of the beam coupling measured at FE34. Expected values based on independent pinhole and LOCO measurements are also reported for comparison.

values are obtained under the assumption that the beam coupling at NCD-SWEET is the same as the beam coupling at FE34, though this might not exactly be the case in a real operational scenario [31]. In Fig. 11, the horizontal error bars in data and the shaded area of the reference values stem from a 15% relative uncertainty in the beam coupling calculations at FE34. Vertical error bars stem from the dispersion of data around the fitted curves given by Eq. (23), as reported for example in Fig. 10.

The measured horizontal beam size is roughly the same for the four different couplings and all values are compatible with theoretical predictions within the experimental uncertainties. This quantitatively proves that the coupling scan does not appreciably influence the horizontal beam size at the undulator location. The average value of 124 μm is in excellent agreement with the expected value of 129 μm.

On the contrary, the vertical beam size increases with the coupling from (4.6 ± 1.4) μm at $\kappa = 0.50\%$ to (14.0 ± 1.2) μm at $\kappa = 2.80\%$. Data are in good agreement with expectations. The relatively large uncertainties at low couplings stem from the limited range of transverse displacements Δy probed with the current experimental setup: at the NCD-SWEET beamline, the maximum distance is limited to $z_{\rm max} = 1.2$ m due to mechanical restrictions. Experimental uncertainties can be reduced, and even smaller beam size can in principle be measured, by accessing larger distances to better probe the large coherence areas, as described in Eq. (4).

Regarding the effects of possible instabilities on beam size measurements, we cannot exclude that mechanical vibrations and source instabilities at frequencies higher than the inverse of the exposure time might influence the vertical beam size estimations and uncertainties. An optimal value of the exposure time of 10 ms or less would be required to measure the instantaneous source size without most vibration effects. In our case, however, the exposure time of 50 ms is limited by the signal-to-noise ratio (the average count on the camera is 400). In this view, the technique will definitely benefit from higher fluxes in higher-energy machines and from state-of-the-art detectors, besides achieving the high-accuracy and finesse typical of statistical methods [16].

TABLE II. Measured horizontal and vertical coherence lengths $\sigma^{H,V}_{\rm coh}$, horizontal and vertical electron beam sizes obtained via the Van Cittert and Zernike formalism $\sigma^{H,V}_{\rm beam,VCZ}$, horizontal and vertical electron beam sizes obtained with the LUT formalism $\sigma^{H,V}_{\rm beam,LUT}$, and expected values $\sigma^{H,V}_{\rm beam,th}$ based on independent pinhole and LOCO measurements.

Coupling at FE34	$\sigma^H_{\rm coh}$ [μm]	$\sigma^H_{\rm beam,VCZ}$ [μm]	$\sigma^H_{\rm beam,LUT}$ [μm]	$\sigma^H_{\rm beam,th}$ [μm]
$\kappa = 0.50\%$	4.2 ± 0.2	125 ± 6	125 ± 6	129
$\kappa = 0.65\%$	4.3 ± 0.2	122 ± 6	122 ± 6	129
$\kappa = 1.60\%$	4.1 ± 0.2	126 ± 6	126 ± 6	129
$\kappa = 2.80\%$	4.3 ± 0.2	122 ± 6	122 ± 6	129
	$\sigma^V_{\rm coh}$ [μm]	$\sigma^V_{\rm beam,VCZ}$ [μm]	$\sigma^V_{\rm beam,LUT}$ [μm]	$\sigma^V_{\rm beam,th}$ [μm]
$\kappa = 0.50\%$	105 ± 32	5.0 ± 1.5	4.6 ± 1.4	5.5
$\kappa = 0.65\%$	66 ± 13	8.0 ± 1.6	7.4 ± 1.5	6.2
$\kappa = 1.60\%$	44 ± 6	11.9 ± 1.6	11.4 ± 1.6	9.8
$\kappa = 2.80\%$	36.0 ± 3	14.6 ± 1.2	14.0 ± 1.2	12.9

Finally, it is worth mentioning the comparison between the two models for the undulator source. By applying the Van Cittert and Zernike theorem, the vertical beam sizes are larger with respect to the full simulations. A difference in the order of 10% arises at $\kappa = 0.50\%$, which progressively reduces to roughly 4% at $\kappa = 2.80\%$. The two models perfectly agree along the horizontal direction. This suggests that the Van Cittert and Zernike theorem applies when the undulator source size is sufficiently large (as evident along the horizontal direction and along the vertical direction for large coupling values), whereas deviations from the rigorous statistical optics approach arise for very small beam sizes, as also reported in [16,34]. We could not evidence these differences given the current resolution limit of the setup and the uncertainties in the reference values, and accuracy levels in the order of a few percents are required to discriminate between the two models. However, this might be of interest in future light sources for accurate measurements of small beam sizes.

V. CONCLUSIONS

We have shown how to perform full 2D beam size measurements with the HNFS technique. The method relies on Fourier analysis of heterodyne speckles to assess the 2D transverse coherence properties of the incoming x rays. The electron beam sizes along the horizontal and vertical directions are then retrieved by means of precomputed LUTs based on rigorous statistical optics approaches.

After reviewing the underlying physical principles of the technique, we thoroughly describe the effects of the limited resolution of the detection system, as well as the peculiar near-field effects generating the so-called Talbot oscillations. This allows to introduce a data reduction procedure that is fully self-consistent.

The method has been applied at the hard x-ray undulator beamline NCD-SWEET at the ALBA Synchrotron Light Source. To test the sensitivity of the technique to different beam sizes, the beam coupling in the machine has been changed using four different settings of the skew quadrupoles, resulting in different vertical beam sizes of a few micrometers at the NCD-SWEET source point.

We show that the measured horizontal beam size does not vary with the coupling. The average value of 124 μm is in excellent agreement with the expected value of 129 μm. Opposite to this case, the vertical beam size increases as a function of the beam coupling from roughly 5 μm at coupling $\kappa = 0.50\%$ up to 14 μm at coupling $\kappa = 2.80\%$, in good agreement with expectations.

To the authors knowledge, this experimentally proves for the first time that the HNFS technique can resolve beam sizes as small as 5 μm, thus drastically improving on past measurements reported in the literature and making the technique a suitable diagnostics for low-emittance particle beams.

ACKNOWLEDGMENTS

The authors would like to especially thank C. Kamma-Lorger for her help during the first experiments, and M. Malfois for his continuous comprehension and support while using the beamline. Furthermore, the authors are grateful for the support from the ALBA Engineering and Control Room teams for their help.

[1] H. Wiedemann, *Particle Accelerator Physics* (Springer, Berlin, 2007).

[2] G. Kube, Review of synchrotron radiation based diagnostics for transverse profile measurements, in *Proceedings of the 8th European Workshop on Beam Diagnostics and Instrumentation for Particle Accelerators, DIPAC 2007*, Venice, Italy (JACoW, Venice, 2007).

[3] K. A. Nugent, Coherent methods in the x-ray sciences, Adv. Phys. **59**, 1 (2010).

[4] P. Elleaume, C. Fortgang, C. Penel, and E. Tarazona, Measuring beam sizes and ultrasmall electron emittances using an x-ray pinhole camera, J. Synchrotron Radiat. **2**, 209 (1995).

[5] C. Thomas, G. Rehm, I. Martin, and R. Bartolini, X-ray pinhole camera resolution and emittance measurement, Phys. Rev. ST Accel. Beams **13**, 022805 (2010).

[6] N. Samadi, X. Shi, L. Dallin, and D. Chapman, Source size measurement options for low-emittance light sources, Phys. Rev. Accel. Beams **23**, 024801 (2020).

[7] M. A. Tordeux, L. Cassinari, O. Chubar, J. C. Denard, D. Pedeau, and B. Pottin, Ultimate resolution of Soleil x-ray pinhole camera, in *Proceedings of DIPAC 07, Venice, Italy* (2007), https://accelconf.web.cern.ch/d07/papers/TUPC16.pdf.

[8] F. Ewald, Comparison of beam size monitoring using x rays at ESRF, *Workshop on Emittance Measurements for Light Sources and FELs*, https://indico.cells.es/event/128/.

[9] T. Mitsuhashi, Beam profile and size measurement by SR interferometers, in *Beam Measurement: Proceedings of the Joint US-CERN-Japan-Russia School on Particle Accelerators, Montreux and Geneva, Switzerland* (World Scientific, Singapore, 1999).

[10] L. Torino and U. Iriso, Transverse beam profile reconstruction using synchrotron radiation interferometry, Phys. Rev. Accel. Beams **19**, 122801 (2016).

[11] T. Naito and T. Mitsuhashi, Very small beam size measurement by a reflective synchrotron radiation interferometer, Phys. Rev. ST Accel. Beams **9**, 122802 (2006).

[12] W. Leitenberger, H. Wendrock, L. Bischoff, and T. Weitkamp, Pinhole interferometry with coherent hard x rays, J. Synchrotron Radiat. **11**, 190 (2004).

[13] M. Lyubomirskiy, I. Snigireva, and A. Snigirev, Lens coupled tunable Young's double pinhole system for hard x-ray spatial coherence characterization, Opt. Express **24**, 13679 (2016).

[14] F. Ferri, D. Magatti, D. Pescini, M. A. C. Potenza, and M. Giglio, Heterodyne near-field scattering: A technique for complex fluids, Phys. Rev. E **70**, 041405 (2004).

[15] R. Cerbino, L. Peverini, M. A. C. Potenza, A. Robert, P. Bosecke, and M. Giglio, X-ray-scattering information obtained from near-field speckle, Nat. Phys. **4**, 238 (2008).

[16] M. D. Alaimo, M. A. C. Potenza, M. Manfredda, G. Geloni, M. Sztucki, T. Narayanan, and M. Giglio, Probing the Transverse Coherence of an Undulator X-ray Beam Using Brownian Particles, Phys. Rev. Lett. **103**, 194805 (2009).

[17] M. D. Alaimo *et al.*, Mapping the transverse coherence of the self-amplified spontaneous emission of a free-electron laser with the heterodyne speckle method, Opt. Express **22**, 30013 (2014).

[18] Y. Kashyap, H. Wang, and K. Sawhney, Two-dimensional transverse coherence measurement of hard-x-ray beams using near-field speckle, Phys. Rev. A **92**, 033842 (2015).

[19] M. Siano, B. Paroli, E. Chiadroni, M. Ferrario, and M. A. C. Potenza, Measurement of power spectral density of broad-spectrum visible light with heterodyne near field scattering and its scalability to betatron radiation, Opt. Express **23**, 32888 (2015).

[20] M. Siano, B. Paroli, M. A. C. Potenza, U. Iriso, A. A. Nosych, L. Torino, S. Mazzoni, G. Trad, and A. N. Goldblatt, Characterizing temporal coherence of visible synchrotron radiation with heterodyne near field speckles, Phys. Rev. Accel. Beams **20**, 110702 (2017).

[21] M. Siano, B. Paroli, and M. A. C. Potenza, Heterodyne near field speckles: From laser light to x rays, Adv. Phys. X **6**, 1891001 (2021).

[22] J. W. Goodman, *Statistical Optics* (John Wiley & Sons, Inc., New York, 2000).

[23] M. Born and E. Wolf, *Principles of Optics* (Pergamon Press, Oxford, 1970).

[24] L. Mandel and E. Wolf, *Optical Coherence and Quantum Optics* (Cambridge University Press, Cambridge, 1995).

[25] A. Hofmann, *The Physics of Synchrotron Radiation* (Cambridge University Press, Cambridge, England, 2005).

[26] H. C. Van de Hulst, *Light Scattering by Small Particles* (Dover Publications, Inc., New York, 1981).

[27] J. W. Goodman, *Introduction to Fourier Optics* (Ben Roberts & Company, Englewood, 2007).

[28] S. Mazzoni, M. A. C. Potenza, M. D. Alaimo, S. J. Veen, M. Dielissen, E. Leussink, J.-L. Dewandel, O. Minster, E. Kufner, G. Wegdam, and P. Schall, SODI-COLLOID: A combination of static and dynamic light scattering on board the International Space Station, Rev. Sci. Instrum. **84**, 043704 (2013).

[29] M. A. C. Potenza, K. P. V. Sabareesh, M. Carpineti, M. D. Alaimo, and M. Giglio, How to Measure the Optical Thickness of Scattering Particles from the Phase Delay of Scattered Waves: Application to Turbid Samples, Phys. Rev. Lett. **105**, 193901 (2010).

[30] https://uspas.fnal.gov/materials/09UNM/Unit_11_Lecture_18_Synchrotron_radiation.pdf.

[31] A. Franchi, L. Farvacque, J. Chavanne, F. Ewald, B. Nash, K. Scheidt, and R. Tomas, Vertical emittance reduction and preservation in electron storage rings via resonance driving terms correction, Phys. Rev. ST Accel. Beams **14**, 034002 (2011).

[32] U. Iriso, M. Alvarez, F. Fernandez, F. Perez, and A. Olmos, Diagnostics during the ALBA storage ring commissioning, in *Proceedings of the 10th European Workshop on Beam Diagnostics and Instrumentation for Particle Accelerators, DIPAC 2011, Hamburg, Germany* (JACoW, Hamburg, 2011).

[33] G. Geloni, E. Saldin, E. Schneidmiller, and M. Yurkov, Transverse coherence properties of x-ray beams in third-generation synchrotron radiation sources, Nucl. Instrum. Methods Phys. Res., Sect. A **588**, 463 (2008).

[34] C. Thomas, P. Dudin, and M. Hoesch, Coherence of a near diffraction limited undulator synchrotron radiation source, Opt. Commun. **359**, 171 (2016).

[35] G. Geloni, S. Serkez, R. Khubbutdinov, V. Kocharyan, and E. Saldin, Effects of energy spread on brightness and coherence of undulator sources, J. Synchrotron Radiat. **25**, 1335 (2018).

[36] M. Siano, B. Paroli, M. A. C. Potenza, U. Iriso, C. S. Kamma-Lorger, A. A. Nosych, S. Mazzoni, and G. Trad, Electron beam size measurements using the heterodyne near field speckles at ALBA, in *Proceedings of the 8th International Beam Instrumentation Conference, IBIC 2019, Malmo, Sweden* (JACoW, Malmo, 2019).

[37] O. Chubar and P. Elleaume, Accurate and efficient computation of synchrotron radiation in the near field region, in *Proceedings of the 6th European Particle Accelerator Conference, Stockholm, 1998* (IOP, London, 1998), pp. 1177–1179.

[38] O. Chubar, Recent updates in the Synchrotron Radiation Workshop code, on-going developments, simulation activities, and plans for the future, in *Proceedings of the SPIE 9209, Advances in Computational Methods for X-ray Optics III* (SPIE, San Diego, 2014), p. 920907.

[39] J. Safranek, Experimental determination of storage ring optics using orbit response measurements, Nucl. Instrum. Methods Phys. Res., Sect. A **388**, 27 (1997).

[40] J. Safranek, G. Portmann, A. Terebilo, and C. Steier, MATLAB-based LOCO, in *Proceedings of the 8th European Particle Accelerator Conference, Paris, 2002* (EPS-IGA and CERN, Geneva, 2002).

[41] G. Benedetti, D. Einfeld, Z. Marti, and M. Munoz, LOCO in the ALBA storage ring, in *Proceedings of the 2nd International Particle Accelerator Conference, San Sebastián, Spain* (EPS-AG, Spain, 2011).